
Free-T2M: Frequency Enhanced Text-to-Motion Diffusion Model With Consistency Loss

Wenshuo Chen^{*123} Haozhe Jia^{*123} Songning Lai¹³ Keming Wu⁴³ Hongru Xiao⁵ Lijie Hu⁶ Yutao Yue¹³

Abstract

Rapid progress in text-to-motion generation has been largely driven by diffusion models. However, existing methods focus solely on temporal modeling, thereby overlooking frequency-domain analysis. We identify two key phases in motion denoising: the **semantic planning stage** and the **fine-grained improving stage**. To address these phases effectively, we propose **Frequency enhanced text-to-motion diffusion model (Free-T2M)**, incorporating stage-specific consistency losses that enhance the robustness of static features and improve fine-grained accuracy. Extensive experiments demonstrate the effectiveness of our method. Specifically, on StableMoFusion, our method reduces the FID from **0.189** to **0.051**, establishing a new SOTA performance within the diffusion architecture. These findings highlight the importance of incorporating frequency-domain insights into text-to-motion generation for more precise and robust results. The code and visualization results can be found on the [website](#).

1. Introduction

In recent years, text-to-motion (T2M) generation has seen significant advancements, driven by the emergence of powerful generative modeling techniques. Among these, diffusion models have demonstrated remarkable potential in various domains, including image generation (He & Wang, 2024; Ho et al., 2020; Ning et al., 2024), audio synthesis (Kong et al., 2021; Huang et al., 2022), and video generation (Ho et al., 2022; Blattmann et al., 2023). Their inherent ability to handle complex, high-dimensional data distributions makes diffusion models particularly well-suited for T2M

tasks (Tevet et al., 2022; Chen et al., 2023; Huang et al., 2024; Zhang et al., 2023b; Dai et al., 2024). By leveraging the stochastic nature of diffusion processes, these models excel at capturing the diverse and multimodal mapping relationships between textual descriptions and motion data. This has enabled substantial progress in practical applications such as animation, virtual reality, and human-computer interaction, where generating realistic and contextually coherent human motions is of critical importance.

However, despite these advancements, current T2M models primarily focus on temporal sequence modeling. This limited perspective overlooks the fact that human motion inherently exhibits multi-frequency patterns, with different body parts operating at distinct frequencies to achieve coordinated movements. The lack of explicit frequency-domain analysis in these models can result in generated motions that fail to capture the natural rhythm and coordination observed in human actions. Furthermore, existing methods typically adopt general-purpose diffusion techniques without tailoring them to address the unique challenges posed by motion generation, such as maintaining physical plausibility and semantic consistency (chen et al., 2024; Cen et al., 2024; Lin et al., 2024). These limitations underscore the need for a deeper understanding of the interplay between temporal and frequency-domain features in text-to-motion generation, hindering the development of more accurate and reliable motion synthesis approaches.

Previous work has identified instability issues when handling semantically similar textual perturbations, revealing the lack of robustness and reliability in current models, significant limitations for real-world applications (chen et al., 2024). They have addressed this problem by focusing on attention mechanisms and adversarial training methods. However, these approaches can compromise model accuracy and are ineffective for models that use non-CLIP-based text encoders (Jiang et al., 2023; Radford et al., 2021). In contrast, our work investigates the denoising mechanisms of diffusion models from a frequency-domain perspective, providing a more interpretable solution grounded in the model’s generative process, which ultimately improves performance.

In Figure 1, we observe that during the early stages of the diffusion denoising process, when the data is heavily cor-

^{*}Equal contribution ¹HKUST(GZ) ²Shandong University ³Deep Interdisciplinary Intelligence Lab ⁴Tsinghua University ⁵Tongji University ⁶KAUST. Correspondence to: Yutao Yue <yutaoyue@hkust-gz.edu.cn>.

This work was supported by Guangzhou-HKUST(GZ) Joint Funding Program Grant No.2023A03J0008, Education Bureau of Guangzhou Municipality.

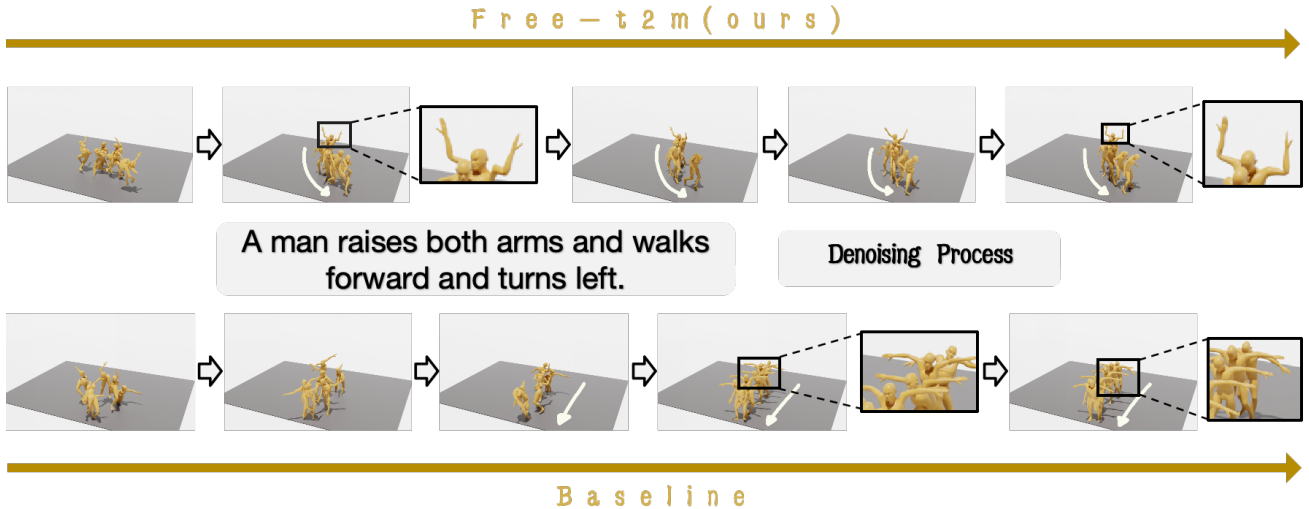


Figure 1. T2M Denoising Mechanism. The white arrows represent motion trajectories. At the beginning of the denoising process, the input is pure Gaussian noise. During the early stages, the model first generates low-frequency semantic motion information. As the denoising steps progress, fine-grained details such as hand and leg movements are gradually synthesized. We observed that errors in generating early semantic information tend to propagate through subsequent steps, leading to catastrophic errors in the fine-grained optimization process.

rupted by noise, the model primarily focuses on recovering low frequency components of the motion data (Qian et al., 2024). These low frequency components correspond to the broad, semantic aspects of motion, such as the type of action being performed (e.g., moving in a circle without hands or legs movement) and are crucial for capturing the overall structure of the motion. High-frequency components, which represent fine-grained details of movement, are typically recovered in the later stages of denoising.

We analyze the root cause of catastrophic errors in motion sequences: the failure of semantic planning in the early stages. Once semantic planning goes wrong, no matter how detailed the subsequent generation is, the result will still be an incorrect motion. Therefore, to enhance the robustness of semantic generation, it is crucial to minimize errors occurring in the early stages, ensuring a solid foundation for the subsequent generation process. In this paper, we propose a **Low Frequency Consistency Guidance** to enhance the accuracy in the early stage. By applying the Discrete Cosine Transform (DCT) (Ning et al., 2024) to both generated and real motion data, we extract the low frequency components and compute a low frequency loss that quantifies the discrepancy between them. This loss serves as a reward signal that guides the model to prioritize the accurate reconstruction of essential semantic information during the early denoising stages. By emphasizing low frequency components, we ensure that the generated motions capture the correct overall actions and avoid semantic errors that could lead to unrealistic results. In motion data, low-frequency information

plays a dominant role (Cen et al., 2024; Lin et al., 2024; Mahmood et al., 2019b). Overemphasizing high-frequency information can lead to instability during training. On this basis, we propose **Semantic Consistency Guidance** (Li et al., 2024a) in the later stages of generation as a replacement for high-frequency detail consistency guidance. Intuitively, when the generated motion aligns more closely with the input prompt: capturing fine-grained descriptors such as "wave hands slowly" or "move legs swiftly". We consider the high-frequency details to be well-reflected. At the same time, this approach prevents core semantic information, such as "walk" or "jump", from being disrupted during the later stages of the process. We leverage motion-to-text (M2T) models (Guo et al., 2022b), which are capable of extracting semantic representations from motion data by mapping motions to textual descriptions. By computing the cosine similarity between the semantic embeddings of the generated motions and those of the ground truth motions, we construct a semantic reward that encourages the model to produce motions that are semantically consistent with the desired actions. Our main contributions can be summarized as follows:

- Distinguished from previous works that primarily focused on temporal aspects, We introduce a novel research perspective by analyzing motion generation from a denoising process
- We propose two types of consistency loss that act on the semantic planning and fine-grained improving stages, significantly improving model stability and precision.

- Extensive experiments demonstrate the effectiveness of our approach. Without increasing model complexity, our method achieves state-of-the-art performance, thereby facilitating practical applications in text-to-motion generation.

2. Related Work

Text Conditioned Human Motion Diffusion Generation.

Recent advancements in text-conditioned human motion generation have been driven by diffusion models (Tevet et al., 2022; Zhang et al., 2023b; Huang et al., 2024; Zhang et al., 2022; Chen et al., 2023; Dai et al., 2024), which have shown remarkable potential in modeling the complex relationships between textual inputs and motion sequences. Prominent works include MotionDiffuse (Zhang et al., 2022), which leverages cross-attention for text integration; MDM (Tevet et al., 2022), which explores diverse denoising networks such as Transformer and GRU; and PhysDiff (Yuan et al., 2023), which incorporates physical constraints to enhance realism. While ReMoDiffuse (Zhang et al., 2023b) improves performance through retrieval mechanisms, MotionLCM (Dai et al., 2024) achieves real-time, controllable generation via a latent consistency model. Despite these advances, existing methods often struggle with capturing both low-frequency semantic structures and high-frequency motion details, which are critical for generating coherent and realistic human motions.

Moreover, diffusion models in motion generation often lack tailored designs for the intrinsic properties of motion data. For example, the denoising process may fail to prioritize low-frequency components that define the overall motion trajectory, leading to semantic inconsistencies in the generated outputs (Mahmood et al., 2019b; Tevet et al., 2022). Furthermore, the reliance on generic architectures (Li et al., 2024b; Hu et al., 2024) limits their ability to address domain-specific challenges, such as robust handling of complex text prompts and preserving temporal coherence.

3. Method

3.1. Preliminaries

The diffusion model generation process can be divided into three stages: a **forward process**, which progressively diffuses noise into the data sample; a **reverse process**, where a network is optimized to remove added noise and recover the original signal; and an **inference process**, which employs the trained network to iteratively denoise noisy samples.

In the forward diffusion process, noise is incrementally introduced to the data x_0 to yield x_t , modeled as:

$$q(x_t|x_{t-1}) = \mathcal{N}(x_t; \sqrt{1 - \beta_t}x_{t-1}, \beta_t\mathbf{I}), \quad (1)$$

and, equivalently in the frequency domain:

$$X_t(f) = \sqrt{\bar{\alpha}_t}X_0(f) + \sqrt{1 - \bar{\alpha}_t}\epsilon(f), \quad (2)$$

where $\bar{\alpha}_t$ and $\epsilon(f)$ represent the preserved signal strength and Gaussian noise in the frequency domain, respectively. Notably, during this process, the high-frequency components of the motion data are disrupted first, followed by the low-frequency components.

Theorem 3.1. *In diffusion models, low-frequency components are recovered earlier than high-frequency components during the reverse denoising process (Qian et al., 2024). Formally, given a motion signal in the frequency domain $\hat{m}_t(\omega)$, the signal-to-noise ratio (SNR) at frequency ω is defined as:*

$$SNR(\omega) = \frac{|\hat{m}_0(\omega)|^2}{\int_0^t g^2(s) ds} \quad (3)$$

where $\hat{m}_0(\omega)$ is the initial power spectral density of the motion signal and $\int_0^t g^2(s) ds$ represents the accumulated noise energy. For higher frequencies ω_H , the SNR decreases more rapidly than for lower frequencies ω_L , i.e.,

$$SNR(\omega_H) < SNR(\omega_L), \quad \forall \omega_H > \omega_L. \quad (4)$$

As a result, low-frequency components are restored first, providing a semantic foundation for the subsequent recovery of high-frequency details. (Please refer to Appendix B.2 for the detailed proof)

In the reverse process (motion generation), the model starts from pure noise x_T and iteratively removes noise to reconstruct the original motion. Initially, only low-frequency information, such as broad motion trajectories, is recovered due to the noise’s predominance. As t decreases, the noise level reduces, allowing the model to gradually restore high-frequency details and finer motion features.

Theorem 3.2. *In the reverse denoising process of diffusion models for motion generation, the accurate restoration of high-frequency components depends explicitly on the consistent reconstruction of low-frequency components.*

Let $\hat{m}_t(\omega)$ denote the motion signal at timestep t in the frequency domain, where ω represents the frequency. For high-frequency components ω_H and low-frequency components ω_L , the recovery of $\hat{m}_{t-1}(\omega_H)$ is conditioned on the accurate reconstruction of $\hat{m}_{t-1}(\omega_L)$:

$$p(\hat{m}_{t-1}(\omega_H) | \hat{m}_t(\omega_H), \hat{m}_t(\omega_L)) \approx p(\hat{m}_{t-1}(\omega_H) | \hat{m}_{t-1}(\omega_L)) \quad (5)$$

where the Markov property of the diffusion process implies that the reconstruction of ω_H at time $t - 1$ strongly depends on the low-frequency foundation $\hat{m}_{t-1}(\omega_L)$.

Furthermore, since the signal-to-noise ratio (SNR) for high frequencies is significantly lower than for low frequencies:

$$SNR(\omega_H) < SNR(\omega_L), \quad \forall \omega_H > \omega_L \quad (6)$$

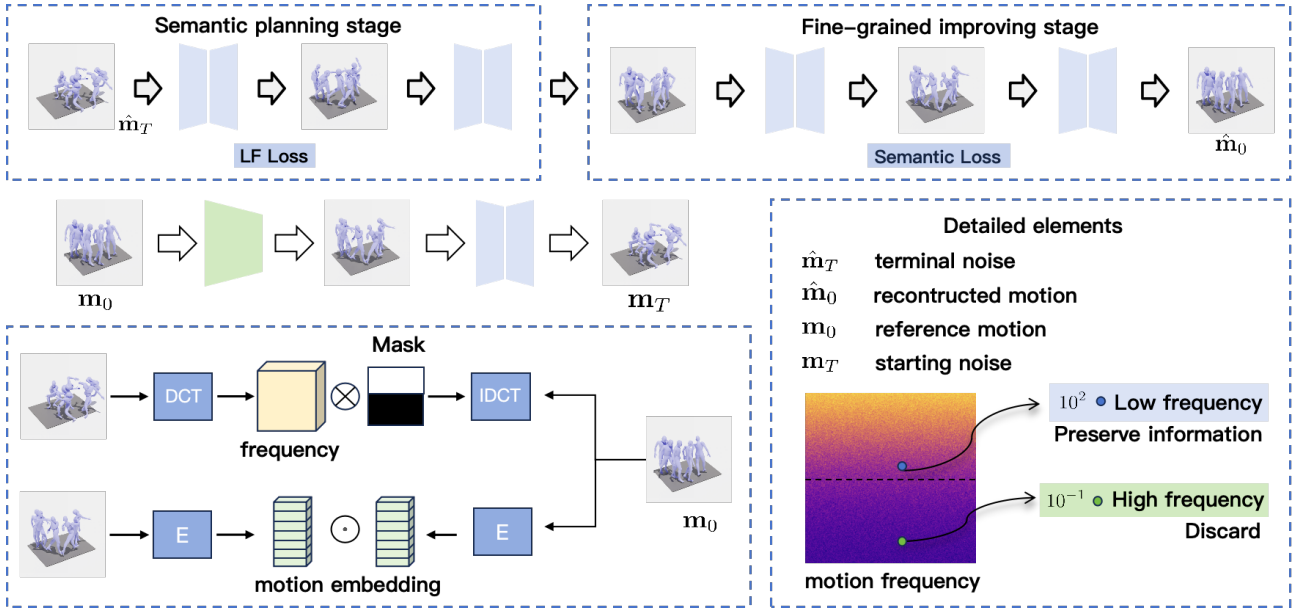


Figure 2. **Overview of the Free-T2M framework.** Free-T2M employs a two-stage denoising process: low-frequency reconstruction and semantic planning. The low-frequency consistency loss (LF Loss) ensures the accurate recovery of global semantic structure, while the semantic loss aligns detailed motion with the textual description and the reference motion m_0 using motion embeddings. Frequency-domain operations via Discrete Cosine Transform (DCT) prioritize low-frequency components to preserve semantics, while high-frequency details are progressively reconstructed to enhance motion fidelity.

the high-frequency components are more corrupted and rely on the restored low-frequency components for meaningful reconstruction. This dependency ensures semantic consistency in motion semantics and spatial coherence (Please refer to Appendix B.3 for the detailed proof).

Based on this observation, we propose our method. First, we employ a **low-frequency loss** to align the fundamental low-frequency components of the motion, which often encode essential attributes such as the general direction of torso movement. High-frequency information, while crucial for detailed motion, is not directly aligned. This is due to two reasons: (1) high-frequency components contribute only a small proportion of the motion data (B.2), and (2) high-frequency details strongly depend on low-frequency structure (B.3). Thus, by ensuring the alignment of low-frequency components, the high-frequency components are naturally better preserved. To further enhance high-frequency accuracy, we introduce a **semantic consistency loss** that ensures generated motions align with human language descriptions. This approach bridges the gap between low-frequency alignment and the generation of semantically meaningful, high-fidelity motion. We further discuss in the section 4.5 why we use semantic consistency loss instead of directly using high-frequency consistency loss.

3.2. Low-Frequency Consistency

We propose a **Low-Frequency Consistency Guidance** method that focuses on enhancing the model’s capability to generate accurate low-frequency components. This is achieved by designing a low-frequency compensation loss function using the discrete cosine transform (DCT) and its inverse (IDCT). The DCT transforms data from the time domain into the frequency domain, allowing us to isolate low-frequency components. Let $m_0 \in \mathbb{R}^{N \times D}$ denote the real motion data, where N represents the number of frames and D indicates the number of features per frame. Furthermore, let $\hat{m}_0 \in \mathbb{R}^{N \times D}$ represent the motion data generated by the diffusion model.

For each feature dimension $d = 1, 2, \dots, D$ and a sequence x_0 of length N , the Discrete Cosine of m_0 at index k is given by:

$$c_{m_0}^d[k] = \alpha(k) \sum_{n=0}^{N-1} m_0^d[n] \cos\left(\frac{\pi(2n+1)k}{2N}\right) \quad (7)$$

where m_0^d and \hat{m}_0^d are the sequences of the d -th feature in all frames. The $k = 0, 1, \dots, N-1$, and the normalization

factor $\alpha(k)$ is defined as:

$$\alpha(k) = \begin{cases} \sqrt{\frac{1}{N}}, & \text{if } k = 0 \\ \sqrt{\frac{2}{N}}, & \text{if } k > 0 \end{cases} \quad (8)$$

We select the first K coefficients (corresponding to the low frequencies):

$$L_{m_0}^d = c_{m_0}^d[1 : K] \quad (9)$$

$$L_{\hat{m}_0}^d = c_{\hat{m}_0}^d[1 : K] \quad (10)$$

Then pad the low-frequency coefficients with zeros to match the original length N , then apply IDCT:

$$\tilde{m}_0^d = \text{IDCT}(\underbrace{[L_{m_0}^d, 0, \dots, 0]}_K, \underbrace{0, \dots, 0}_{N-K}) \quad (11)$$

$$\tilde{\hat{m}}_0^d = \text{IDCT}(\underbrace{[L_{\hat{m}_0}^d, 0, \dots, 0]}_K, \underbrace{0, \dots, 0}_{N-K}) \quad (12)$$

The loss functions can be defined between the reconstructed low-frequency sequences:

$$\mathcal{L}_{\text{LF}}^{\text{L1}} = \frac{1}{N \cdot D} \sum_{d=1}^D \sum_{i=1}^N |\tilde{m}_0^{d,i} - \tilde{\hat{m}}_0^{d,i}| \quad (13)$$

3.3. Semantic Consistency

We measure the semantic similarity between the original text T and the generated motion \hat{T} embedded in the text, which is embedded by the text-to-motion model using the cosine similarity of their semantic embeddings. Let $\phi(T)$ and $\phi(\hat{T})$ denote the embedding vectors of T and \hat{T} .

The cosine similarity S is computed as:

$$S = \cos(\phi(T), \phi(\hat{T})) = \frac{\phi(T)^\top \phi(\hat{T})}{\|\phi(T)\| \|\phi(\hat{T})\|} \quad (14)$$

where $\|\cdot\|$ denotes the Euclidean norm.

where F is the M2T conversion function with parameters θ_F .

The **Semantic Loss** \mathcal{L}_S is a function designed to encourage higher semantic similarity between T and \hat{T} . We define $R(S)$ as:

$$\mathcal{L}_S = \max\{0, S - S_{\text{th}}\} \quad (15)$$

This function rewards the model when the similarity surpasses S_{th} and provides no reward otherwise.

Given that high-frequency information degrades first and low-frequency information is prioritized for reconstruction

during diffusion processes 1, we design a mask-based strategy applying $\mathcal{L}_{\text{LF}}^{\text{L1}}$ early and \mathcal{L}_S later to ensure semantic consistency and detail accuracy.

$$\text{mask}_{\text{LF}}(t) = \begin{cases} 1, & \text{if } t \leq T_{\text{LF}}, \\ 0, & \text{otherwise,} \end{cases} \quad (16)$$

$$\text{mask}_S(t) = \begin{cases} 0, & \text{if } t \leq T_{\text{LF}}, \\ 1, & \text{otherwise.} \end{cases}$$

Thus the combined loss can be defined as:

$$\mathcal{L} = \lambda_1 \mathcal{L}_{\text{simple}} + \lambda_2 \mathcal{L}_{\text{LF}}^{\text{L1}} \cdot \text{mask}_{\text{LF}} - \lambda_3 \mathcal{L}_S \cdot \text{mask}_S \quad (17)$$

Where $\mathcal{L}_{\text{simple}}$ is the traditional loss of the diffusion model, **mask** can make the loss work in specific time steps during the denoise process.

Algorithm 1 Free-T2M

Input: Real motion m_0 , Generated motion \hat{m}_0 , Text T , Generated embedding \hat{T} , Low-frequency coefficient count K , Frames N , Features D , Weights $\lambda_1, \lambda_2, \lambda_3$, Threshold S_{th} , Masks $\text{mask}_{\text{LF}}, \text{mask}_S$

Output: Combined loss \mathcal{L}_{all}

Step 1: Low-Frequency Consistency Loss

for $d = 1$ **to** D **do**

 Compute DCT: $c_{m_0}^d = \text{DCT}(m_0^d)$, $c_{\hat{m}_0}^d = \text{DCT}(\hat{m}_0^d)$

 Select K coefficients: $L_{m_0}^d = c_{m_0}^d[1 : K]$, $L_{\hat{m}_0}^d = c_{\hat{m}_0}^d[1 : K]$

 Reconstruct signals via IDCT:

$\tilde{m}_0^d = \text{IDCT}([L_{m_0}^d, 0, \dots, 0])$,

$\tilde{\hat{m}}_0^d = \text{IDCT}([L_{\hat{m}_0}^d, 0, \dots, 0])$

end for

 Compute L1 loss: $\mathcal{L}_{\text{LF}}^{\text{L1}} = \frac{1}{N \cdot D} \sum_{d=1}^D \sum_{i=1}^N |\tilde{m}_0^{d,i} - \tilde{\hat{m}}_0^{d,i}|$

Step 2: Semantic Consistency Loss

 Compute embeddings: $\phi(T)$, $\phi(\hat{T})$

 Compute cosine similarity: $S = \frac{\phi(T)^\top \phi(\hat{T})}{\|\phi(T)\| \|\phi(\hat{T})\|}$

 Loss: $R(S) = -\max\{0, S - S_{\text{th}}\}$

Step 3: Combined Loss

 Traditional loss: $\mathcal{L}_{\text{simple}}$

 Combine: $\mathcal{L} = \lambda_1 \mathcal{L}_{\text{simple}} + \lambda_2 \mathcal{L}_{\text{LF}}^{\text{L1}} \cdot \text{mask}_{\text{LF}} - \lambda_3 R(S) \cdot \text{mask}_S$

Return: \mathcal{L}

4. Experiment

We evaluate our approach on two popular motion-language benchmarks: HumanML3D (Guo et al., 2022a) and KIT-ML (Plappert et al., 2016). The HumanML3D dataset comprises 14,616 motions sourced from AMASS (Mahmood et al.,

Method	Venue	FID ↓	R-Precision ↑			Diversity →
			top1	top2	top3	
Real		0.002±0.000	0.511±0.003	0.703±0.003	0.797±0.002	9.503±0.065
MLD (Chen et al., 2023)	CVPR 2023	0.473±0.013	0.481±0.003	0.673±0.003	0.772±0.002	9.724±0.082
ReMoDiffuse (Zhang et al., 2023b)	ICCV 2023	0.103±0.004	0.510±0.005	0.698±0.006	0.795±0.004	9.018±0.075
MotionDiffuse (Zhang et al., 2022)	TPAMI 2024	0.630±0.001	0.491±0.001	0.681±0.001	0.782±0.001	9.410±0.049
MotionLCM (Dai et al., 2024)	ECCV 2024	0.467±0.012	0.502±0.003	0.701±0.002	0.803±0.002	9.361±0.660
T2M-GPT (Zhang et al., 2023a)	CVPR 2023	0.141±0.005	0.492±0.003	0.679±0.002	0.775±0.002	9.722±0.082
MDM _{50steps} (Baseline) (Tevet et al., 2022)	ICLR 2023	0.544±0.044	0.320±0.005	0.498±0.004	0.611±0.007	9.559±0.086
MDM _{1000steps} (Baseline) (Tevet et al., 2022)	ICLR 2023	0.548±0.085	0.313±0.006	0.472±0.007	0.601±0.005	9.464±0.067
StableMoFusion (Baseline) (Huang et al., 2024)	ACM MM 2024	0.189±0.003	0.499±0.004	0.680±0.006	0.779±0.007	9.466±0.002
Free-MDM _{50steps} (Ours)	-	0.256±0.045	0.466±0.008	0.657±0.007	0.757±0.005	9.666±0.080
Free-MDM _{1000steps} (Ours)	-	0.370±0.030	0.435±0.005	0.621±0.007	0.722±0.009	9.450±0.066
Free-StableMoFusion (Ours)	-	0.051±0.002	0.520±0.013	0.707±0.003	0.803±0.006	9.480±0.005

Table 1. Evaluation metrics for HumanML3D dataset. \pm indicates a 95% confidence interval. Red and Blue indicate the best and the second best result. The right arrow \rightarrow means the closer to real motion the better. Our method has achieved accuracy improvements on two baseline. Red and Blue indicate the best and the second best result. Our method has achieved accuracy (FID \downarrow) improvements on two baseline, and the FID of Free-StableMoFusion has reached the SOTA for the text to motion task in the diffusion architecture.

2019a) and HumanAct12 (Guo et al., 2020), each paired with three textual descriptions, resulting in a total of 44,970 descriptions. This dataset encompasses a wide range of actions, such as walking, exercising, and dancing. The KIT-ML dataset, on the other hand, includes 3,911 motions and 6,278 text descriptions, serving as a smaller-scale evaluation benchmark. For both datasets, we employ the pose representation used in T2M-GPT. Motions are augmented through mirroring and split into training, validation, and testing sets with a ratio of 0.8 : 0.15 : 0.05. (Zhang et al., 2023a; Guo et al., 2023)

Evaluation Metrics. In addition to the commonly utilized metrics such as Frechet Inception Distance (FID), R-Precision, Multimodal Distance (MM-Dist), and Diversity, which are employed by T2M-GPT (Zhang et al., 2023a). Furthermore, human evaluation is employed to obtain accuracy and human preference results for the outputs generated by the model.

- **Frechet Inception Distance (Heusel et al., 2017) (FID):** We can evaluate the overall motion quality by measuring the distributional difference between the high-level features of the motions.
- **R-Precision:** We rank Euclidean distances between a given motion sequence and 32 text descriptions (1 ground-truth and 31 randomly selected mismatched descriptions). We report Top-1, Top-2, and Top-3 accuracy of motion-to-text retrieval.
- **Diversity:** From a set of motions, we randomly sample 300 pairs and compute the average Euclidean distances between them to measure motion diversity.
- **Human Evaluation:** We conducted evaluations of each model’s generated results in the form of a Google Form. We collected user ratings on model prediction, which en-

compassed both the quality and correctness of the generated motions. Additionally, we analyzed user preferences for model prediction. Further details will be discussed in section 4.3.

4.1. Experimental Setup

We adopt model architecture settings similar to those of MDM and StableMoFusion. For MDM, the batch size is set to 64, and the AdamW (Loshchilov & Hutter, 2019) optimizer is employed. Our models are trained using two different noising step configurations: $T = 1000$ and $T = 50$, with a cosine noise schedule. The total number of iterations is fixed at 600,000, with a learning rate of 1×10^{-4} . The hyperparameters λ_1 , λ_2 , and λ_3 are set to 1.0, 1.0, and 0.5. For StableMoFusion, we follow its training methodology, running for 200,000 steps. The hyperparameters λ_1 , λ_2 , and λ_3 are set to 1.0, 0.5, and 2.0, respectively. The entire training process can be executed on a single RTX 3090 GPU with 24 GB of memory.

4.2. Comparison with Baseline

We evaluated our model on the HumanML3D and KIT datasets, comparing its performance to baseline models, including StableMoFusion and MDM (Table 1 and Table 2). For MDM, our approach achieved significant improvements in both accuracy (R-precision **0.611** \rightarrow **0.757**) and precision (FID **0.544** \rightarrow **0.256**) in HumanML3D dataset. On StableMoFusion, our method improved the FID from 0.189 to 0.051, while also achieving enhancements across all three R-Precision metrics. Similarly, on KIT-ML, our method achieved notable improvements in accuracy.

Additionally, we compared our method with ReModiffuse (Zhang et al., 2023b), MotionLCM (Dai et al., 2024), Mo-

Method	Venue	FID ↓	R-Precision ↑			Diversity →
			top1	top2	top3	
Real		0.031±0.004	0.424±0.005	0.649±0.006	0.779±0.006	11.08±0.097
MLD (Chen et al., 2023)	CVPR 2023	0.404±0.027	0.390±0.008	0.609±0.008	3.204±0.027	10.80±0.117
ReMoDiffuse (Zhang et al., 2023b)	ICCV 2023	0.155±0.006	0.427±0.014	0.641±0.004	0.765±0.055	10.80±0.105
MotionDiffuse (Zhang et al., 2022)	TPAMI 2024	1.954±0.062	0.417±0.004	0.621±0.004	0.739±0.004	11.100±0.163
T2M-GPT (Zhang et al., 2023a)	CVPR 2023	0.514±0.029	0.416±0.006	0.627±0.006	0.745±0.006	10.921±0.108
MDM _{50steps} (baseline) (Tevet et al., 2022)	ICLR 2023	0.497±0.021	0.164±0.004	0.291±0.004	0.396±0.004	10.847±0.109
MDM _{1000steps} (baseline) (Tevet et al., 2022)	ICLR 2023	0.556±0.0698	0.322±0.019	0.431±0.013	0.698±0.052	10.73±0.201
StableMoFusion (baseline) (Huang et al., 2024)	ACM MM 2024	0.258±0.029	0.445±0.006	0.660±0.005	0.782±0.004	10.936±0.077
Free-MDM _{50steps} (Ours)	-	0.401±0.033	0.382±0.006	0.587±0.006	0.707±0.007	10.733±0.102
Free-MDM _{1000steps} (Ours)	-	0.529±0.036	0.377±0.004	0.579±0.007	0.705±0.006	10.826±0.117
Free-StableMoFusion(Ours)	-	0.155±0.079	0.431±0.003	0.671±0.001	0.789±0.002	10.902±0.045

Table 2. Quantitative results on the KIT-ML test set. Red and Blue indicate the best and the second best result. The right arrow → means the closer to real motion the better. Our method has achieved accuracy improvements on two baseline. Red and Blue indicate the best and the second best result. Our method has achieved accuracy (FID↓) improvements on two baseline.

Method	FID ↓	R-Precision ↑		
		top1	top2	top3
$\mathcal{L}_{LF} + \mathcal{L}_S$	0.261±0.043	0.466±0.008	0.657±0.007	0.757±0.005
\mathcal{L}_{LF} only	0.444±0.003	0.456±0.004	0.652±0.001	0.759±0.001
\mathcal{L}_S only	0.731±0.066	0.4305±0.007	0.619±0.006	0.722±0.006

Table 3. Ablation experiment results of MDM_{50steps} for \mathcal{L}_{LF} and \mathcal{L}_S on the HumanML3D test set. Bold indicates the best result.

Method	ACC	Preference
MDM	0.580	0.412
MDM(ours)	0.650	0.588
StableMoFusion	0.644	0.384
StableMoFusion(ours)	0.724	0.616

Table 4. Human Evaluation Results. We randomly sampled 100 test texts for manual evaluation of correctness and user preference. The results demonstrate that our method improves model accuracy and garners higher user preference.

tionDiffuse (Zhang et al., 2022), and T2M-GPT (Zhang et al., 2023a). The results demonstrate that our Free-StableMoFusion achieves state-of-the-art (SOTA) performance in accuracy. These findings further validate the effectiveness of our method and its plug-and-play capabilities.

4.3. Human Evaluation

We randomly sampled 100 text entries from the HumanML3D Test dataset, and under the same random seed and other parameter settings, we used Free-MDM (ours), MDM, Free-StableMoFusion (ours), and StableMoFusion to generate corresponding motions for visualization. Five different evaluators anonymously compared the visualized outputs with the ground truth (GT) in a pairwise manner for manual evaluation. Evaluators were asked to assess the correctness of the motions and rank the models based on naturalness, accuracy, and completeness to select the better-performing model. The results are shown in the Tab. 4.2.

Method	FID ↓	Top-3
MDM	0.713±0.023	0.676±0.006
MDM (Ours)	0.467±0.080	0.682±0.004
Stable MoFusion	0.202±0.050	0.660±0.006
Stable MoFusion (Ours)	0.165±0.046	0.703±0.005

Table 5. Comparison of robustness testing for MDM and Stable-MoFusion across different metrics (FID, R-Precision) on the test set.

Our model demonstrated a significant improvement in accuracy, with increases of 7% and 8% over MDM and Stable-MoFusion, respectively. Additionally, a greater number of users preferred the results generated by our model, with an advantage of 17.6% over MDM and 22.8% over Stable-MoFusion. Despite our model exhibiting lower R-precision on StableMoFusion, from a human perception perspective, our model was still preferred. Overall, our approach better maintains low-frequency consistency in generating the subject’s semantics, while enhanced semantic consistency improves the generation of finer details without disrupting the low-frequency components. This highlights the effectiveness of our method. More details can be seen in Appendix H.

4.4. Ablation Study

In Table 3, We conducted comprehensive ablation studies to validate the effectiveness of our proposed method. In the first experiment, we evaluated the contributions of the two loss functions: \mathcal{L}_{LF} and \mathcal{L}_S . When applying only \mathcal{L}_{LF} , the FID achieved was 0.444, indicating its strong ability to preserve low-frequency consistency in the results. On the other hand, applying only \mathcal{L}_S yielded an FID of 0.731 but demonstrated a significant improvement in R-Precision (Top-3) from 0.611 to 0.722, highlighting its effectiveness in improving semantic alignment.

The results further demonstrated that the combination of \mathcal{L}_{LF} and \mathcal{L}_S achieved the best overall performance. This synergy

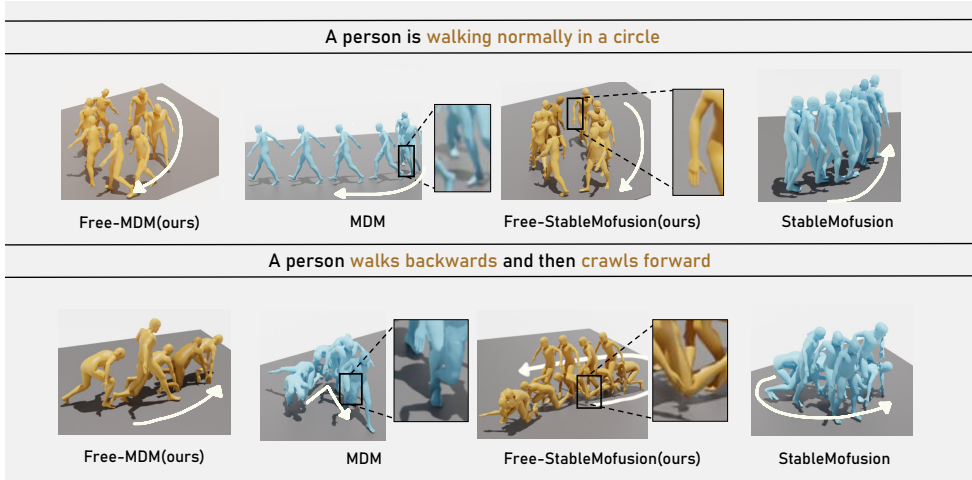


Figure 3. Visualization results. The white arrows represent motion trajectories. In several examples, the baseline model produces errors in low-frequency information, leading to incorrect trajectories and ultimately affecting the accuracy of the motion. Our model demonstrates superior semantic consistency and finer-grained local actions compared to the baseline.

indicates that the two losses address complementary aspects of the optimization, leading to high-quality results both visually and semantically. These findings underscore the effectiveness and adaptability of our method, showcasing its capacity to balance fidelity and semantic consistency effectively.

4.5. Why Not High Frequency Consistency?

In this paper, we utilize a low-frequency consistency loss during the early stages of denoising to enhance the accuracy of low-frequency semantic modeling. In the later stages, we focus primarily on generating high-frequency details. However, when directly applying high-frequency consistency loss (L_h), we encounter issues where the model struggles to fit the data and even fails during training (Table 6).

We identify two possible reasons for this problem: First, due to the low-frequency nature of motion data, high-frequency features in motion are sparse. Overemphasizing high-frequency consistency can lead to instability during training. Second, placing excessive emphasis on high-frequency features can disrupt the originally generated low-frequency features, resulting in errors in the output.

To address these issues, we propose using semantic consistency loss as a substitute for high-frequency loss in the later stages of denoising. Semantic consistency loss emphasizes alignment with semantics during the later denoising stages. It incorporates both low-frequency semantics, such as "walk" and "circle," and fine-grained descriptions like "move leg fast" or "walk slowly." This approach effectively optimizes high-frequency details while preserving the original low-frequency features, achieving a balanced and robust improvement in motion generation.

Method	FID ↓	R-Precision ↑		
		top1	top2	top3
StableMoFusion (Baseline)	0.189±0.003	0.499±0.004	0.680±0.006	0.779±0.007
Free-StableMoFusion (our)	0.051±0.002	0.520±0.013	0.707±0.003	0.803±0.006
StableMoFusion (L_h)	11.581±0.002	0.129±0.011	0.224±0.004	0.309±0.041

Table 6. High Frequency Consistency Loss Ablation Study. When directly aligning high-frequency information, the sparsity of motion high-frequency data and its dependency on low-frequency information can lead to training failure.

4.6. Robustness Analysis

Following SATO (chen et al., 2024), robustness is a critical challenge for T2M models. To address this, we utilized the SATO perturbed text dataset, which involves synonym replacements in the text while preserving its length and meaning. This dataset simulates diverse expressions of the same intent by different users interacting with the model.

The test results, as shown in Table 5, demonstrate that our method outperforms baseline models on both FID and R-Precision under text perturbations across two models. This indicates that our approach enhances the model’s robustness to some extent, aligning with the motivation behind our method. By incorporating the low-frequency consistency loss, the model becomes more stable in capturing low-frequency semantic information, leading to improved accuracy. With accurate low-frequency information in place, the high-frequency information, which depends on the low-frequency context, is better modeled, resulting in more precise generation of details such as hand and leg movements.

5. Conclusion

In this paper, we propose the plug-and-play Free-T2M framework, which leverages an analysis of the denoising

mechanism and incorporates two consistency losses to optimize the denoising process. Our approach achieves more robust and accurate results across various baselines, setting new state-of-the-art performance within the diffusion architecture.

Due to the limitations of the current M2T model’s performance, semantic consistency is easily affected by the model’s inherent biases. In the future, we can further improve motion-language alignment to enhance the effectiveness of our approach.

References

- Blattmann, A., Dockhorn, T., Kulal, S., Mendelevitch, D., Kilian, M., Lorenz, D., Levi, Y., English, Z., Voleti, V., Letts, A., Jampani, V., and Rombach, R. Stable video diffusion: Scaling latent video diffusion models to large datasets, 2023. URL <https://arxiv.org/abs/2311.15127>.
- Cen, Z., Pi, H., Peng, S., Shen, Z., Yang, M., Zhu, S., Bao, H., and Zhou, X. Generating human motion in 3d scenes from text descriptions, 2024. URL <https://arxiv.org/abs/2405.07784>.
- chen, W., Xiao, H., Zhang, E., Hu, L., Wang, L., Liu, M., and Chen, C. Sato: Stable text-to-motion framework. In *Proceedings of the 32nd ACM International Conference on Multimedia*, MM ’24, pp. 6989–6997. ACM, October 2024. doi: 10.1145/3664647.3681034. URL <http://dx.doi.org/10.1145/3664647.3681034>.
- Chen, X., Jiang, B., Liu, W., Huang, Z., Fu, B., Chen, T., Yu, J., and Yu, G. Executing your commands via motion diffusion in latent space, 2023. URL <https://arxiv.org/abs/2212.04048>.
- Dai, W., Chen, L.-H., Wang, J., Liu, J., Dai, B., and Tang, Y. Motionlcm: Real-time controllable motion generation via latent consistency model, 2024. URL <https://arxiv.org/abs/2404.19759>.
- Guo, C., Zuo, X., Wang, S., Zou, S., Sun, Q., Deng, A., Gong, M., and Cheng, L. Action2motion: Conditioned generation of 3d human motions. In *Proceedings of the 28th ACM International Conference on Multimedia*, pp. 2021–2029, 2020.
- Guo, C., Zou, S., Zuo, X., Wang, S., Ji, W., Li, X., and Cheng, L. Generating diverse and natural 3d human motions from text. In *Proceedings of the IEEE/CVF Conference on Computer Vision and Pattern Recognition (CVPR)*, pp. 5152–5161, June 2022a.
- Guo, C., Zuo, X., Wang, S., and Cheng, L. Tm2t: Stochastic and tokenized modeling for the reciprocal generation of 3d human motions and texts, 2022b. URL <https://arxiv.org/abs/2207.01696>.
- Guo, C., Mu, Y., Javed, M. G., Wang, S., and Cheng, L. Momask: Generative masked modeling of 3d human motions, 2023. URL <https://arxiv.org/abs/2312.00063>.
- He, Z. and Wang, Y.-H. Ddim sampling for generative aibim, a faster intelligent structural design framework, 2024. URL <https://arxiv.org/abs/2412.20899>.
- Heusel, M., Ramsauer, H., Unterthiner, T., Nessler, B., and Hochreiter, S. Gans trained by a two time-scale update rule converge to a local nash equilibrium. In Guyon, I., Luxburg, U. V., Bengio, S., Wallach, H., Fergus, R., Vishwanathan, S., and Garnett, R. (eds.), *Advances in Neural Information Processing Systems*, volume 30. Curran Associates, Inc., 2017. URL https://proceedings.neurips.cc/paper_files/paper/2017/file/8a1d694707eb0fefe65871369074926d-Paper.pdf.
- Ho, J., Jain, A., and Abbeel, P. Denoising diffusion probabilistic models, 2020. URL <https://arxiv.org/abs/2006.11239>.
- Ho, J., Salimans, T., Gritsenko, A., Chan, W., Norouzi, M., and Fleet, D. J. Video diffusion models, 2022. URL <https://arxiv.org/abs/2204.03458>.
- Hu, M., Zhu, M., Zhou, X., Yan, Q., Li, S., Liu, C., and Chen, Q. Efficient text-driven motion generation via latent consistency training, 2024. URL <https://arxiv.org/abs/2405.02791>.
- Huang, R., Lam, M. W. Y., Wang, J., Su, D., Yu, D., Ren, Y., and Zhao, Z. Fastdiff: A fast conditional diffusion model for high-quality speech synthesis, 2022. URL <https://arxiv.org/abs/2204.09934>.
- Huang, Y., Yang, H., Luo, C., Wang, Y., Xu, S., Zhang, Z., Zhang, M., and Peng, J. Stablemofusion: Towards robust and efficient diffusion-based motion generation framework, 2024. URL <https://arxiv.org/abs/2405.05691>.
- Jiang, B., Chen, X., Liu, W., Yu, J., Yu, G., and Chen, T. Motiongpt: Human motion as a foreign language, 2023. URL <https://arxiv.org/abs/2306.14795>.
- Kong, Z., Ping, W., Huang, J., Zhao, K., and Catanzaro, B. Diffwave: A versatile diffusion model for audio synthesis, 2021. URL <https://arxiv.org/abs/2009.09761>.

- Langley, P. Crafting papers on machine learning. In Langley, P. (ed.), *Proceedings of the 17th International Conference on Machine Learning (ICML 2000)*, pp. 1207–1216, Stanford, CA, 2000. Morgan Kaufmann.
- Li, M., Yang, T., Kuang, H., Wu, J., Wang, Z., Xiao, X., and Chen, C. Controlnetplusplus: Improving conditional controls with efficient consistency feedback. In *European Conference on Computer Vision (ECCV)*, 2024a.
- Li, M., Zhai, C., Yao, S., Xie, Z., Chen, K., and Jiang, Y.-G. Infinite motion: Extended motion generation via long text instructions, 2024b. URL <https://arxiv.org/abs/2407.08443>.
- Lin, J., Zeng, A., Lu, S., Cai, Y., Zhang, R., Wang, H., and Zhang, L. Motion-x: A large-scale 3d expressive whole-body human motion dataset, 2024. URL <https://arxiv.org/abs/2307.00818>.
- Loper, M., Mahmood, N., Romero, J., Pons-Moll, G., and Black, M. J. SMPL: A skinned multi-person linear model. *ACM Trans. Graphics (Proc. SIGGRAPH Asia)*, 34(6): 248:1–248:16, October 2015.
- Loshchilov, I. and Hutter, F. Decoupled weight decay regularization, 2019. URL <https://arxiv.org/abs/1711.05101>.
- Mahmood, N., Ghorbani, N., Troje, N. F., Pons-Moll, G., and Black, M. J. AMASS: Archive of motion capture as surface shapes. In *International Conference on Computer Vision*, pp. 5442–5451, October 2019a.
- Mahmood, N., Ghorbani, N., Troje, N. F., Pons-Moll, G., and Black, M. J. Amass: Archive of motion capture as surface shapes, 2019b. URL <https://arxiv.org/abs/1904.03278>.
- Ning, M., Li, M., Su, J., Jia, H., Liu, L., Beneš, M., Salah, A. A., and Ertugrul, I. O. Dctdiff: Intriguing properties of image generative modeling in the dct space, 2024. URL <https://arxiv.org/abs/2412.15032>.
- Plappert, M., Mandery, C., and Asfour, T. The kit motion-language dataset. *Big Data*, 4(4):236–252, December 2016. ISSN 2167-647X. doi: 10.1089/big.2016.0028. URL <http://dx.doi.org/10.1089/big.2016.0028>.
- Qian, Y., Cai, Q., Pan, Y., Li, Y., Yao, T., Sun, Q., and Mei, T. Boosting diffusion models with moving average sampling in frequency domain, 2024. URL <https://arxiv.org/abs/2403.17870>.
- Radford, A., Kim, J. W., Hallacy, C., Ramesh, A., Goh, G., Agarwal, S., Sastry, G., Askell, A., Mishkin, P., Clark, J., Krueger, G., and Sutskever, I. Learning transferable visual models from natural language supervision, 2021. URL <https://arxiv.org/abs/2103.00020>.
- Sposini, V., Grebenkov, D. S., Metzler, R., Oshanin, G., and Seno, F. Universal spectral features of different classes of random-diffusivity processes. *New Journal of Physics*, 22(6):063056, June 2020. ISSN 1367-2630. doi: 10.1088/1367-2630/ab9200. URL <http://dx.doi.org/10.1088/1367-2630/ab9200>.
- Tevet, G., Raab, S., Gordon, B., Shafir, Y., Cohen-Or, D., and Bermano, A. H. Human motion diffusion model, 2022. URL <https://arxiv.org/abs/2209.14916>.
- Yang, X., Zhou, D., Feng, J., and Wang, X. Diffusion probabilistic model made slim, 2022. URL <https://arxiv.org/abs/2211.17106>.
- Yuan, Y., Song, J., Iqbal, U., Vahdat, A., and Kautz, J. Physdiff: Physics-guided human motion diffusion model, 2023. URL <https://arxiv.org/abs/2212.02500>.
- Zhang, J., Zhang, Y., Cun, X., Huang, S., Zhang, Y., Zhao, H., Lu, H., and Shen, X. T2m-gpt: Generating human motion from textual descriptions with discrete representations, 2023a. URL <https://arxiv.org/abs/2301.06052>.
- Zhang, M., Cai, Z., Pan, L., Hong, F., Guo, X., Yang, L., and Liu, Z. Motiondiffuse: Text-driven human motion generation with diffusion model, 2022. URL <https://arxiv.org/abs/2208.15001>.
- Zhang, M., Guo, X., Pan, L., Cai, Z., Hong, F., Li, H., Yang, L., and Liu, Z. Remodiffuse: Retrieval-augmented motion diffusion model, 2023b. URL <https://arxiv.org/abs/2304.01116>.

A. Overview of Appendix

The Appendix is organized into the following sections:

- Section B: Derivation and Proof.
- Section C: Evaluation Metrics.
- Section D: Efficiency Analysis.
- Section E: More Visualization Results.
- Section F: Motion Data Analysis.
- Section G: More Experiments, including loss coefficient ablation, different training methods, R-Precision under different sample sizes, mask strategy ablation.
- Section H: Details of Human Evaluation.

B. Derivation and Proof

B.1. Power Spectral Density in Diffusion Process

Theorem B.1 (Power Spectral Density in Diffusion Process). *In the forward diffusion process, the spectral density of the power $S_{\mathbf{m}_t}(\omega)$ of the motion signal \mathbf{m}_t at time t can be expressed as:*

$$S_{\mathbf{m}_t}(\omega) = |\hat{\mathbf{m}}_0(\omega)|^2 + \int_0^t g^2(s)ds, \quad (18)$$

where $|\hat{\mathbf{m}}_0(\omega)|^2$ is the initial power spectral density of the motion signal, and $\int_0^t g^2(s)ds$ represents the accumulated noise energy in the frequency domain.

In the Time Domain, the forward diffusion process of Diffusion (Sposini et al., 2020) is defined as :

$$d\mathbf{m}_t = \mathbf{f}(\mathbf{m}_t, t)dt + g(t)d\mathbf{w}_t \quad (19)$$

where $\mathbf{f}(\mathbf{m}_t, t)$ is the drift coefficient, $g(t)$ is the diffusion coefficient, and \mathbf{w}_t is the Wiener process. Assuming $\mathbf{f}(\mathbf{m}_t, t) = 0$, the integral form becomes:

$$\mathbf{m}_t = \mathbf{m}_0 + \int_0^t g(s)d\mathbf{w}_s \quad (20)$$

Applying the discrete Fourier transform (DFT) to \mathbf{m}_t , we obtain:

$$\hat{\mathbf{m}}_t(\omega) = \hat{\mathbf{m}}_0(\omega) + \hat{\epsilon}_t(\omega) \quad (21)$$

Where, $\hat{\mathbf{m}}_t(\omega)$ denotes the frequency-domain representation of \mathbf{m}_t , $\hat{\mathbf{m}}_0(\omega)$ represents the initial frequency-domain representation of the clean motion signal \mathbf{m}_0 , and $\hat{\epsilon}_t(\omega)$ corresponds to the frequency-domain representation of the noise term ϵ_t .

The noise term ϵ_t in the time domain is:

$$\epsilon_t(x) = \int_0^t g(s)d\mathbf{w}_s \quad (22)$$

Using the autocorrelation property of the Wiener process, the expected value of the noise energy is:

$$\mathbb{E}[\epsilon_t(x)\epsilon_t(y)] = \begin{cases} \int_0^t g^2(s)ds, & x = y, \\ 0, & x \neq y \end{cases} \quad (23)$$

The Fourier transform of $\epsilon_t(x)$ yields:

$$\mathbb{E}[|\hat{\epsilon}_t(\omega)|^2] = \int_0^t g^2(s)ds \quad (24)$$

So, the power spectral density $S_{\mathbf{m}_t}(\omega)$ of the motion signal \mathbf{m}_t is defined as:

$$S_{\mathbf{m}_t}(\omega) = \mathbb{E}[|\hat{\mathbf{m}}_t(\omega)|^2] \quad (25)$$

Substituting $\hat{\mathbf{m}}_t(\omega) = \hat{\mathbf{m}}_0(\omega) + \hat{\epsilon}_t(\omega)$, we expand:

$$\mathbb{E}[|\hat{\mathbf{m}}_t(\omega)|^2] = \mathbb{E}[|\hat{\mathbf{m}}_0(\omega)|^2 + 2 \operatorname{Re}(\hat{\mathbf{m}}_0(\omega)\hat{\epsilon}_t^*(\omega)) + |\hat{\epsilon}_t(\omega)|^2] \quad (26)$$

Since $\mathbb{E}[\hat{\epsilon}_t(\omega)] = 0$ and $\mathbb{E}[\hat{\mathbf{m}}_0(\omega)\hat{\epsilon}_t^*(\omega)] = 0$, the cross-term vanishes, leaving:

$$S_{\mathbf{m}_t}(\omega) = |\hat{\mathbf{m}}_0(\omega)|^2 + \mathbb{E}[|\hat{\epsilon}_t(\omega)|^2] \quad (27)$$

Substituting $\mathbb{E}[|\hat{\epsilon}_t(\omega)|^2] = \int_0^t g^2(s)ds$, we arrive at:

$$S_{\mathbf{m}_t}(\omega) = |\hat{\mathbf{m}}_0(\omega)|^2 + \int_0^t g^2(s)ds \quad (28)$$

This derivation demonstrates that the power spectral density of the motion signal at time t comprises two components: the original signal power $|\hat{\mathbf{m}}_0(\omega)|^2$ and the noise power accumulated over time $\int_0^t g^2(s) ds$.

B.2. Spectral Analysis in Diffusion-Based Motion Generation

In the forward diffusion process for motion generation, high-frequency components are corrupted earlier than low-frequency components, while in the reverse denoising process, low-frequency components are reconstructed first, providing the semantic foundation for high-frequency recovery (Yang et al., 2022). Formally:

Given an initial motion signal \mathbf{m}_0 , the power spectral density of the corrupted signal \mathbf{m}_t at time t (B.1) is expressed as

$$S_{\mathbf{m}_t}(\omega) = |\hat{\mathbf{m}}_0(\omega)|^2 + \int_0^t g^2(s) ds, \quad (29)$$

where $|\hat{\mathbf{m}}_0(\omega)|^2 \propto |\omega|^{-\alpha}$ with $\alpha > 0$, characterizing the low-pass nature of the motion data. The signal-to-noise ratio (SNR) at frequency ω is given by

$$\operatorname{SNR}(\omega) = \frac{|\hat{\mathbf{m}}_0(\omega)|^2}{\int_0^t g^2(s) ds}, \quad (30)$$

which reveals that the SNR decreases more rapidly at higher frequencies (ω_H) compared to lower frequencies (ω_L), highlighting the stronger impact of noise on high-frequency components of the motion signal.

Forward Diffusion Process: The forward diffusion process corrupts the initial signal \mathbf{m}_0 by adding Gaussian noise over time. The stochastic differential equation (SDE) is:

$$d\mathbf{m}_t = \mathbf{f}(\mathbf{m}_t, t)dt + g(t)d\mathbf{w}_t, \quad (31)$$

where $\mathbf{f}(\mathbf{m}_t, t)$ is the drift coefficient, $g(t)$ is the diffusion coefficient, and \mathbf{w}_t is the Wiener process. Assuming $\mathbf{f}(\mathbf{m}_t, t) = 0$, the integral form is:

$$\mathbf{m}_t = \mathbf{m}_0 + \int_0^t g(s)d\mathbf{w}_s \quad (32)$$

Applying the discrete Fourier transform (DFT), the frequency-domain representation is:

$$\hat{\mathbf{m}}_t(\omega) = \hat{\mathbf{m}}_0(\omega) + \hat{\epsilon}_t(\omega) \quad (33)$$

where $\hat{\epsilon}_t(\omega)$ is the noise component in the frequency domain.

The energy of $\hat{\epsilon}_t(\omega)$ is:

$$\mathbb{E}[|\hat{\epsilon}_t(\omega)|^2] = \int_0^t g^2(s)ds \quad (34)$$

and the power spectral density of \mathbf{m}_t is:

$$S_{\mathbf{m}_t}(\omega) = |\hat{\mathbf{m}}_0(\omega)|^2 + \mathbb{E}[|\hat{\epsilon}_t(\omega)|^2] \quad (35)$$

Since $|\hat{\mathbf{m}}_0(\omega)|^2 \propto |\omega|^{-\alpha}$ for $\alpha > 0$, high-frequency components have significantly lower energy compared to low-frequency components. As $\int_0^t g^2(s)ds$ increases over time, high-frequency components (ω_H) are dominated by noise earlier than low-frequency components (ω_L).

Reverse Denoising Process: In the reverse process, the model reconstructs \mathbf{m}_t by iteratively reducing noise. The denoising step, exemplified by DDPM (Ho et al., 2020), is :

$$\mathbf{m}_{t-1} = \sqrt{\alpha_{t-1}} \left(\frac{\mathbf{m}_t - \sqrt{1 - \alpha_t} \epsilon_\theta(\mathbf{m}_t, t)}{\sqrt{\alpha_t}} \right) + \sqrt{1 - \alpha_{t-1}} \mathbf{z} \quad (36)$$

where $\epsilon_\theta(\mathbf{m}_t, t)$ is the predicted noise and \mathbf{z} is Gaussian noise.

At high noise levels (early timesteps), the model primarily reconstructs low-frequency components (ω_L) due to their higher SNR:

$$\text{SNR}(\omega_L) > \text{SNR}(\omega_H) \quad (37)$$

As noise reduces (later timesteps), the model can progressively recover high-frequency components (ω_H), which are dependent on the reconstructed low-frequency foundation.

The hierarchical nature of signal recovery, where low frequencies provide the semantic structure and high frequencies refine details, is an inherent property of the diffusion model.

B.2.1. LOW-FREQUENCY PRESERVATION AND HIGH-FREQUENCY RECOVERY IN MOTION GENERATION

In motion generation, low-frequency components encode the semantic structure (e.g., walking or jumping) and must be preserved during early diffusion stages. High-frequency components, encoding fine details, are restored in later stages. Given an SNR threshold γ , the time $t_\gamma(\omega)$ at which SNR reaches γ is defined as:

$$\text{SNR}(\omega) = \frac{|\hat{\mathbf{m}}_0(\omega)|^2}{\int_0^{t_\gamma(\omega)} g^2(s)ds} = \gamma. \quad (38)$$

By solving for $t_\gamma(\omega)$, we can determine the recovery time for specific frequencies. So low-frequency components recover earlier, aligning with the semantic planning phase, while high-frequency components recover later, contributing to fine-grained details.

B.3. Dependency of High-Frequency Components on Low-Frequency Structures in Motion Generation

In the reverse denoising process of diffusion models for motion generation, the accurate restoration of high-frequency motion details depends explicitly on the prior reconstruction of low-frequency semantic structures (Qian et al., 2024). Formally, let $\hat{\mathbf{m}}_t(\omega)$ denote the motion signal at timestep t in the frequency domain, where ω represents the frequency. The recovery of high-frequency components $\hat{\mathbf{m}}_t(\omega_H)$ at frequency ω_H requires conditioned restoration based on the low-frequency components $\hat{\mathbf{m}}_t(\omega_L)$ at frequency ω_L , such that:

$$p(\hat{\mathbf{m}}_{t-1}(\omega_H) \mid \hat{\mathbf{m}}_t(\omega_H), \hat{\mathbf{m}}_t(\omega_L)) \approx p(\hat{\mathbf{m}}_{t-1}(\omega_H) \mid \hat{\mathbf{m}}_{t-1}(\omega_L)) \quad (39)$$

To analyze the dependency, consider the denoising process in diffusion models where motion data evolves from pure noise $\hat{\mathbf{m}}_T(\omega)$ back to the original signal $\hat{\mathbf{m}}_0(\omega)$ through iterative refinement:

$$\hat{\mathbf{m}}_{t-1}(\omega) = \sqrt{\alpha_{t-1}} \left(\frac{\hat{\mathbf{m}}_t(\omega) - \sqrt{1 - \alpha_t} \epsilon_\theta(\hat{\mathbf{m}}_t, t)}{\sqrt{\alpha_t}} \right) + \sqrt{1 - \alpha_{t-1}} \mathbf{z} \quad (40)$$

where ϵ_θ is the neural network's predicted noise, α_t is the noise scaling factor, and \mathbf{z} is Gaussian noise.

Applying a frequency decomposition $\omega = \{\omega_L, \omega_H\}$:

$$\hat{\mathbf{m}}_{t-1}(\omega) = (\hat{\mathbf{m}}_{t-1}(\omega_L), \hat{\mathbf{m}}_{t-1}(\omega_H)) \quad (41)$$

By the Markov property of the diffusion process, the joint distribution can be decomposed:

$$p(\hat{\mathbf{m}}_{t-1}(\omega_L), \hat{\mathbf{m}}_{t-1}(\omega_H) \mid \hat{\mathbf{m}}_t(\omega_L), \hat{\mathbf{m}}_t(\omega_H)) = p(\hat{\mathbf{m}}_{t-1}(\omega_L) \mid \hat{\mathbf{m}}_t(\omega_L)) \cdot p(\hat{\mathbf{m}}_{t-1}(\omega_H) \mid \hat{\mathbf{m}}_{t-1}(\omega_L), \hat{\mathbf{m}}_t(\omega_H)) \quad (42)$$

Due to the dominance of low-frequency components in determining semantic structure, $\hat{\mathbf{m}}_{t-1}(\omega_H)$ strongly depends on the reconstructed $\hat{\mathbf{m}}_{t-1}(\omega_L)$:

$$p(\hat{\mathbf{m}}_{t-1}(\omega_H) \mid \hat{\mathbf{m}}_{t-1}(\omega_L), \hat{\mathbf{m}}_t(\omega_H)) \approx p(\hat{\mathbf{m}}_{t-1}(\omega_H) \mid \hat{\mathbf{m}}_{t-1}(\omega_L)) \quad (43)$$

This reflects the fact that high-frequency details align with low-frequency structures, ensuring consistency in motion semantics and spatial coherence.

Furthermore, noise energy $\mathbb{E}[|\hat{\epsilon}_t(\omega_H)|^2]$ in high frequencies ω_H is significantly higher than that in low frequencies ω_L . This emphasizes that high-frequency components are more corrupted by noise and require low-frequency components for meaningful recovery.

The theorem demonstrates that diffusion-based motion generation inherently follows a hierarchical restoration process, where low-frequency semantic consistency provides the foundation for high-frequency detail recovery.

B.4. Detailed DCT and IDCT Formulas

B.4.1. DISCRETE COSINE TRANSFORM (DCT)

For a signal $\mathbf{v} = \{v[0], v[1], \dots, v[N-1]\}$, the DCT is defined as:

$$\mathbf{v}_f[k] = \alpha(k) \sum_{n=0}^{N-1} v[n] \cos\left(\frac{\pi(2n+1)k}{2N}\right), \quad k = 0, 1, \dots, N-1, \quad (44)$$

where the normalization factor $\alpha(k)$ is:

$$\alpha(k) = \begin{cases} \sqrt{\frac{1}{N}}, & \text{if } k = 0, \\ \sqrt{\frac{2}{N}}, & \text{if } k > 0. \end{cases} \quad (45)$$

B.4.2. INVERSE DISCRETE COSINE TRANSFORM (IDCT)

The original signal \mathbf{v} can be recovered from its DCT coefficients $\mathbf{v}_f = \{v_f[0], v_f[1], \dots, v_f[N-1]\}$ using:

$$v[n] = \sum_{k=0}^{N-1} \alpha(k) v_f[k] \cos\left(\frac{\pi(2n+1)k}{2N}\right), \quad n = 0, 1, \dots, N-1 \quad (46)$$

B.4.3. LOW-FREQUENCY FILTERING IN BATCH PROCESSING

Given a batch $\mathbf{X} \in \mathbb{R}^{B \times N \times D}$, where B is the batch size, N is the time step, and D is the feature dimension, the steps for low-frequency filtering are as follows:

1. Compute the DCT for each feature dimension $d = 1, 2, \dots, D$:

$$\mathbf{x}_{d,f}[k] = \alpha(k) \sum_{n=0}^{N-1} x_d[n] \cos\left(\frac{\pi(2n+1)k}{2N}\right), \quad k = 0, 1, \dots, N-1. \quad (47)$$

2. Retain only the first K coefficients (low frequencies) and set the rest to zero:

$$\mathbf{x}_{d,f}[k] = \begin{cases} \mathbf{x}_{d,f}[k], & k < K, \\ 0, & k \geq K. \end{cases} \quad (48)$$

3. Reconstruct the time-domain signal using IDCT:

$$\tilde{\mathbf{x}}_d[n] = \sum_{k=0}^{N-1} \alpha(k) \mathbf{x}_{d,f}[k] \cos\left(\frac{\pi(2n+1)k}{2N}\right), \quad n = 0, 1, \dots, N-1. \quad (49)$$

4. Concatenate the filtered signals along the feature dimension:

$$\mathbf{X}_{\text{filtered}} = \text{Concat}(\tilde{\mathbf{x}}_1, \tilde{\mathbf{x}}_2, \dots, \tilde{\mathbf{x}}_D) \quad (50)$$

C. Evaluation Metrics

Fréchet Inception Distance (FID). FID is used to measure the difference in distribution between generated motions. We have the following formulas to obtain FID:

$$FID = \|\mu_{gt} - \mu_{pred}\|_2^2 - \text{Tr}(\Sigma_{gt} + \Sigma_{pred} - 2(\Sigma_{gt}\Sigma_{pred})^{1/2}) \quad (51)$$

Here, μ represents the mean, Σ is the covariance matrix, and Tr denotes the trace of a matrix. The smaller the difference, the less susceptible the model is to perturbation.

Diversity. Diversity can measure the diversity of action sequences. A larger value of the metric indicates better diversity in the model. We randomly sample S pairs of motions, denoted as f_i and f'_i . According to (Zhang et al., 2023a), we set S to be 300. We can calculate using the following formula:

$$Diversity = \frac{1}{S} \sum_{i=1}^S \|f_i - f'_i\| \quad (52)$$

D. Efficiency Analysis

The proposed method does not impact the inference speed of the model during generation. However, during training, the addition of two extra loss terms, \mathcal{L}_{LF} and \mathcal{L}_S , introduces an increased computational cost, resulting in a slower training process. Specifically, as shown in Table 7, the computational overhead caused by \mathcal{L}_{LF} is relatively minor, while \mathcal{L}_S leads to a more slowdown due to the invocation of an additional model. Because, the efficiency limitations of the DCT transformation algorithm, combined with the computational demands of the motion embedding mechanism, contribute to the reduced training efficiency. Nevertheless, the overall training time increases by 16.7% for MDM and 12.5% for StableMoFusion, while the proposed method achieves notable improvements in model performance.

Time	MDM	Free-MDM	StableMoFusion	Free-StableMoFusion
Training time	72h	84h	96h	108h
Inference time	0.045s	0.045s	0.036s	0.036s

Table 7. Training Time and Inference Time: We conducted our experiments on an NVIDIA 3090 GPU. Training Time refers to the time required for MDM to complete 600,000 steps and StableMoFusion to complete 200,000 steps. Inference Time represents the average time needed by each of the four models to generate 200 samples.

E. More Visualization Results

More visualization results can be found on the [website](#).

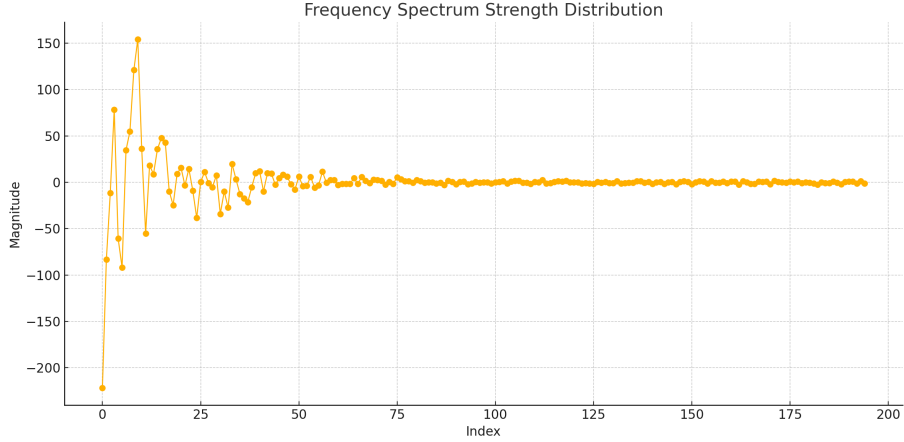


Figure 4. Frequency Spectrum Strength Distribution of Motion Data: This figure illustrates the distribution of motion data after applying the Discrete Cosine Transform (DCT). The results show that motion data is predominantly dominated by low-frequency components, highlighting the importance of focusing on low-frequency information for accurately capturing and generating motion trajectories.

F. Motion Data Analysis

To effectively capture the structural and semantic properties of motion data, we analyze representations commonly used in prior works, focusing on both the *HumanML3D Format* and the *SMPL-based Format*. These representations enable precise motion modeling, providing a robust foundation for text-to-motion generation with enhanced semantic fidelity.

HumanML3D Format. Drawing inspiration from character control techniques, HumanML3D (Cen et al., 2024) encodes motion as a tuple of diverse features, capturing both spatial and dynamic properties. These include root angular velocity r^a (Y-axis), root linear velocities r^x, r^z (XZ-plane), root height r^y , local joint positions $j^P \in \mathbb{R}^{3N_j}$, joint velocities $j^v \in \mathbb{R}^{3N_j}$, joint rotations $j^r \in \mathbb{R}^{6N_j}$, and binary foot-ground contact features $c^f \in \mathbb{R}^4$:

$$x^i = \{r^a, r^x, r^z, r^y, j^P, j^v, j^r, c^f\}. \quad (53)$$

This comprehensive definition encapsulates both high-level semantic structures and fine-grained dynamic details, ensuring a holistic motion representation.

SMPL-based Format. The SMPL model (Loper et al., 2015) emphasizes anatomical accuracy, representing motion through shape parameters β , pose parameters $\theta \in \mathbb{R}^{3 \times 23 + 3}$, and global translation r . Here, θ encodes rotations for 23 joints and a root joint, while β captures individual body shape variations:

$$x^i = \{r, \theta, \beta\}. \quad (54)$$

This format is well-suited for modeling biomechanical realism and is widely used in motion generation tasks.

In addition to leveraging these formats, we introduce a novel frequency-domain perspective to analyze motion data. As illustrated in Figure 4, motion data exhibits a dominance of low-frequency components, which encode broad semantic structures like global trajectories. In contrast, high-frequency components are sparse and primarily capture fine-grained details. This dual-domain analysis lays the groundwork for improving text-to-motion generation by aligning semantic planning with detailed motion refinement.

G. More Experiments

G.1. Loss Coefficient Ablation

The loss coefficients λ_1, λ_2 , and λ_3 correspond to $\mathcal{L}_{\text{simple}}$, \mathcal{L}_{LF} , and \mathcal{L}_{S} , respectively. To determine the optimal values for these coefficients, we conducted experiments with six different parameter combinations, as shown in Table 8.

Our results indicate that the proposed method consistently outperforms the baseline metrics (FID: 0.544, R-Top3: 0.611) across most parameter configurations, demonstrating robust performance under various settings.

λ_1	λ_2	λ_3	FID↓	R-Top3↑
1.0	1.0	1.0	0.431 \pm 0.004	0.736 \pm 0.021
1.0	1.0	0.5	0.256 \pm 0.045	0.757 \pm 0.005
0.5	1.0	1.0	0.301 \pm 0.021	0.728 \pm 0.003
1.0	0.5	1.0	0.471 \pm 0.201	0.733 \pm 0.014
1.0	1.0	0.25	0.398 \pm 0.121	0.755 \pm 0.011
1.0	0.25	1.0	0.592 \pm 0.001	0.701 \pm 0.022
0.25	1.0	1.0	1.134 \pm 0.117	0.607 \pm 0.074

Table 8. Parameter analysis. \pm indicates a 95% confidence interval. R-Top3 represents R-Precision Top3. The table displays the results of three different parameters for loss.

Method	FID ↓	R-Precision ↑		
		top1	top2	top3
StableMoFusion (Baseline)	0.189 \pm 0.003	0.499 \pm 0.004	0.680 \pm 0.006	0.779 \pm 0.007
Free-StableMoFusion (Training)	0.051\pm0.002	0.520 \pm 0.013	0.707 \pm 0.003	0.803 \pm 0.006
Free-StableMoFusion (Fine-tuning)	0.091 \pm 0.011	0.535\pm0.004	0.728\pm0.041	0.819\pm0.002

Table 9. Different training approaches for StableMoFusion: Fine-tuning the existing model using Free-T2M is more efficient and effective.

The best performance was achieved when λ_1 , λ_2 , and λ_3 were set to 1.0, 1.0, and 0.5, respectively, resulting in an FID of 0.256 \pm 0.045 and an R-Top3 of 0.757 \pm 0.005. Notably, reducing λ_1 below 0.5 led to significant model instability, highlighting its critical role in maintaining stable training. For λ_2 , values within the range 0.5 – 1.0 provided robust performance, with higher values yielding improved FID scores. Meanwhile, λ_3 values between 0.25 and 0.5 balanced semantic alignment and generation quality, with higher values contributing positively to semantic consistency.

In summary, our experiments suggest that the optimal range for the loss coefficients is $\lambda_1 \in [0.5, 1.0]$, $\lambda_2 \in [0.5, 1.0]$, and $\lambda_3 \in [0.25, 0.5]$. Within these ranges, the model demonstrates strong robustness and achieves superior performance compared to the baseline.

G.2. Fine-Tuning vs. Training

We investigated two training strategies for our method: training from scratch and fine-tuning on a pre-trained model using our proposed approach. Using StableMoFusion as the baseline, we conducted experiments with both methods. For training from scratch, we set the total training steps to 200,000, while fine-tuning was carried out for 100,000 steps. The results, as presented in Table 9, show that both approaches outperform the baseline, with each offering unique advantages.

Specifically, training from scratch achieved superior performance in FID, while fine-tuning excelled in R-Precision, achieving state-of-the-art results. These findings demonstrate the versatility of our method: it can serve as an effective strategy to enhance performance during the training process for T2M tasks or as a powerful tool to further refine and improve the accuracy of pre-trained models. Furthermore, the exceptional performance of fine-tuning underscores the efficiency of our approach, offering a resource-conscious yet highly effective alternative for performance optimization.

G.3. R-Precision Under Different Sample Sizes.

In most previous works, the sampled texts for R-Precision evaluation consist of 32 candidates (1 ground truth and 31 randomly sampled test texts). The results for Top-1, Top-2, and Top-3 are obtained through ranking and repeated calculations. In this paper, to provide a more rigorous comparison of this metric across different models, we experimented with a broader range of sampled text quantities, using StableMoFusion as the baseline. The results, shown in Table 10, indicate that our method consistently outperforms the baseline across all sampling sizes (8, 16, 32, and 64). This demonstrates that our approach achieves significantly better semantic alignment, further validating its effectiveness.

Method	Num	Top-1	Top-2	Top-3
Real		0.771	0.912	0.962
Free-StableMoFusion	8	0.775	0.923	0.969
StableMoFusion(baseline)		0.753	0.909	0.962
Real		0.646	0.820	0.900
Free-StableMoFusion	16	0.657	0.841	0.913
StableMoFusion(baseline)		0.634	0.816	0.892
Real		0.511	0.703	0.797
Free-StableMoFusion	32	0.520	0.707	0.803
StableMoFusion(baseline)		0.499	0.681	0.779
Real		0.374	0.560	0.672
Free-StableMoFusion	64	0.394	0.566	0.678
StableMoFusion(baseline)		0.378	0.550	0.647

Table 10. R-Precision Results with Different Numbers of Sampled Texts. Our method achieves higher accuracy than the baseline across all sampling sizes, further demonstrating its ability to improve semantic consistency in generated results.

G.4. Mask Strategy Ablation.

An important finding in our work is that the denoising process of diffusion models can be divided into two distinct stages. During the semantic planning stage, we introduce a low-frequency consistency loss, while in the fine-grained improving stage, we propose a semantic consistency loss. Using a mask mechanism, we apply the low-frequency consistency loss only in the early stages and the semantic consistency loss in the later stages. This approach aligns with intuitive reasoning: during the early stages, actions are dominated by disordered noise, making it difficult to capture semantic properties, so applying semantic consistency at this point is ineffective. Conversely, as the denoising process advances into the later stages, low-frequency semantic generation is largely completed. Persistently emphasizing low-frequency generation at this stage would hinder the optimization of high-frequency details. Our experimental results support this rationale (see Table 11). Across two different models, applying the mask strategy consistently improves both accuracy and semantic alignment compared to not using the mask strategy.

Method	FID ↓	R-Precision ↑			Diversity →
		top1	top2	top3	
NO-Mask Free-MDM	0.310 \pm 0.040	0.452 \pm 0.007	0.648 \pm 0.006	0.755 \pm 0.005	9.824 \pm 0.101
Mask Free-MDM	0.261\pm0.043	0.466\pm0.008	0.657\pm0.007	0.757\pm0.005	9.666\pm0.080
No-Mask Free-StableMoFusion	0.103 \pm 0.032	0.491 \pm 0.006	0.673 \pm 0.012	0.769 \pm 0.009	9.110 \pm 0.088
Mask Free-StableMoFusion	0.051\pm0.002	0.520\pm0.003	0.707\pm0.003	0.803\pm0.006	9.480\pm0.005

Table 11. Mask strategy ablation. \pm indicates a 95% confidence interval. Bold text highlights superior results. Across different baselines, the mask strategy can improve model performance, demonstrating the necessity of applying two distinct consistencies during the denoising stages.

H. Details of Human Evaluation

We sampled 100 test texts and manually evaluated the results generated by Free-MDM, MDM, Free-StableMoFusion, and StableMoFusion. Below is the Google Form format we used for the evaluation:

Details of Human Evaluation

[Question1]: Do you think the motion in GIF 1 is correct?

1. Yes
2. No

[Question2]: Do you think the motion in GIF 2 is correct?

1. Yes
2. No

[Question3]: Based on factors such as motion naturalness, semantic alignment, accuracy, and completeness, which motion result do you prefer? (Please consider these criteria holistically when making your choice.)

1. GIF 1
2. GIF 1